

# Complete view of Stark wave-packet evolution

M. B. Campbell, T. J. Bensity, and R. R. Jones

*Department of Physics, University of Virginia, Charlottesville, Virginia 22901*

Picosecond laser pulses have been used to produce Rydberg wave packets in calcium atoms in the presence of a strong static electric field. The dynamics of the Stark wave packets have been observed by measuring the momentum-space probability distribution as a function of time. The full precession of the electronic orbital angular momentum, the appearance of a large-amplitude, linear oscillation of the electronic dipole moment, and a pronounced, periodic up-down asymmetry in the momentum distribution are all observed directly.

A large amount of theoretical and experimental work on Rydberg electron dynamics in a variety of different circumstances has been performed [1]. However, until very recently, the lack of good experimental techniques to monitor the full time-dependent probability distribution of wave packets has severely limited the insight gained from experimental data alone, without the aid of theoretical simulations. Nevertheless, comparisons between the results of experiments and theory have shown that it is possible to produce well-controlled wave packets under a variety of different conditions [1], and that with alternative methods it is possible to experimentally recover their full time-dependent probability distribution with high fidelity [2–4]. In fact, one can now perform dynamics spectroscopy on uncharacterized wave packets. The full electronic motion as viewed in an experiment can be used to interpret the physics behind the motion directly, without relying on theoretical simulations. The refinement of this approach is a necessary prerequisite to controlling wave-packet motion in complex systems where complete quantum mechanical calculations are not readily available.

The results presented in this Rapid Communication provide a complete experimental view of the time-dependent dynamics of a Rydberg wave packet in combined Coulomb and uniform static electric fields. Although numerous experimental studies of Stark wave packets have been performed over the last decade [5–7], this paper describes experiments where the complicated multidimensional evolution of the wave packet can be seen directly. Specifically, the precession of the electronic orbital angular momentum, strong oscillations of the electronic dipole moment along the static field direction, and a periodic asymmetry in the momentum distribution along the static field axis are all linked in the motion of the wave packet and are clearly identified in the measured probability distributions.

In the experiment, ground-state  $4s4s^1S_0$  Ca atoms in a thermal beam are promoted to an intermediate  $4s4p^1P_1$  level using a 5-nsec dye laser pulse. A 1.5-psec laser pulse then drives a fraction of the excited-state atoms into a  $4snd^1D_2$ ,  $26 \leq n \leq 30$  radial Rydberg wave packet [3]. The wave packet is initially localized near the  $\text{Ca}^+$  ion core but immediately propagates radially outward, reflects from the Coulomb potential, and returns to the ion core after one Kepler period,  $\tau_K = 2\pi N^3 = 3.0$  psec [8]. In the absence of the

static field, the wave packet remains localized in an  $\ell=2$  angular-momentum state and exhibits the standard core returns, collapses, and integer and fractional revivals familiar to radial wave packets [1,3].

The presence of a static field, however, destroys the spherical symmetry of the pure Coulomb potential so that angular momentum is no longer conserved. In the frequency domain, the angular-momentum eigenstates corresponding to each principal quantum number mix and form new eigenstates that repel each other, producing the well-known Stark effect [9]. In the time domain, the initial  $d$ -wave packet experiences spatially dependent torques as it moves in the combined Coulomb and Stark potentials, creating a time-dependent distribution of constituent angular-momentum states in the wave packet. In this experiment the static field is applied along the common linear laser polarization axis  $\hat{z}$ , so that there are no torques along  $\hat{z}$  and only  $m_\ell=0$  states contribute. Although cylindrical symmetry reduces the problem to only two dimensions, in the presence of strong fields the wave-packet motion can be quite complex. In our experiments, the applied static field,  $F_S=180$  V/cm, is approximately twice the field at which adjacent Stark manifolds cross and one-third of the field required for static field ionization for the range of Rydberg states under study. The period for angular-momentum precession of the wave packet,  $\tau_S = 2\pi/3F_S N = 54$  psec, for these conditions [5], so that there are approximately 18 Kepler oscillations in each angular-momentum cycle. The separation of the wave-packet motion into radial and angular-momentum oscillations is convenient, but not fully justified due to coupling between these modes.

The electronic evolution is probed using picosecond unipolar, “half-cycle” electric-field pulses (HCPs) [10]. Because the unipolar HCP has a nonzero time-integrated electric field, it delivers a momentum “kick” to the electronic wave packet in the HCP field direction [11]. Ionization occurs if the kick raises the total energy of the wave packet above the saddle point in the combined Coulomb and static-field potential. In the limit of short pulses, the energy transfer depends only on the momentum of the wave packet and the time integral of the HCP field [2,12,13]. By measuring the probability for ionizing the wave packet as a function of time, HCP field amplitude, and HCP polarization, the time-

dependent momentum distribution of the wave packet can be constructed [2,3]. Although small imperfections in the momentum imaging are unavoidable due to the nonzero duration of the HCP and the energy uncertainty in the wave packet [2,3], the experimental distributions capture the dominant features of the wave-packet evolution.

The experimental apparatus and method are essentially identical to those described elsewhere [3,14]. The 1.5-psec, 392-nm laser pulse that excites the  $4snd\ ^1D_2$  wave packet is produced by frequency doubling the 787-nm, 120-fsec output of an amplified, self-mode-locked Ti:sapphire laser in a 3-cm-long KDP crystal. Using state-selective field ionization, we determine that the wave packet has five contributing  $n$  states centered on  $n=28$  ( $N=26.9$ ) with about two-thirds of the population in the  $n=28$  energy level. The atomic and laser beams overlap between two parallel field plates separated by 1.5 cm with +275 V applied to the bottom field plate.

The HCP that probes the wave packet is created by illuminating a biased GaAs photoconductive switch with a portion of the 120-fsec, 787-nm Ti:sapphire laser output [10]. The HCP field amplitude is linearly proportional to the bias voltage on the switch and its polarization direction is parallel to the bias field [10]. The switch is mounted on a rotation stage so that the polarization of the HCP can be rotated continuously about its propagation direction. Nonunipolar features are removed from the pulse by gating the reflectivity of a second, unbiased GaAs wafer with another 120-fsec pulse [10,15]. The “cleaned” HCP probe has a duration of approximately 1 psec, full width at half maximum.

The lasers and HCP counterpropagate along the long dimension of a 0.15-cm by 2.5-cm slit in the upper field plate [3]. The static field pushes ions created by the HCP through the slit towards a microchannel plate detector that is backed by a phosphor screen. The fluorescence from the phosphor is captured by a charge-coupled-device camera and the video output is recorded using a digital oscilloscope [14]. Since the 1.5-psec laser pulse and HCP counterpropagate beneath the slit, atoms experience a relative pulse delay that is approximately 80 psec greater at one end of the slit than at the other. Therefore, by measuring the ionization yield as a function of position, the ionization probability vs delay can be obtained in a single laser shot [14].

The wave-packet ionization probability is measured as a function of HCP field amplitude and delay in a single scan of the GaAs bias voltage. The average video signal from 200 laser shots is discretized into 300 time bins over a 70-psec window at 19 different HCP field amplitudes for each of four HCP field directions,  $\hat{z}$ ,  $-\hat{z}$ ,  $\hat{x}$ , and  $-\hat{x}$ . Since the 1-psec duration of the HCP is significantly less than  $\tau_K$  and  $\tau_S$ , the impulsive momentum retrieval method can be implemented to recover the momentum-space probability distribution of the wave packet [2,3]. At a given delay, the projection of the wave packet’s momentum distribution along the HCP field axis is a scaled derivative of the ionization versus HCP field curve at that time [2].

In order to accurately determine the full probability distribution of the wave packet with a single HCP orientation, the HCP field must be increased to a very high level where the ionization probability saturates at unity. The physical interpretation of the need for such strong fields is straightforward.

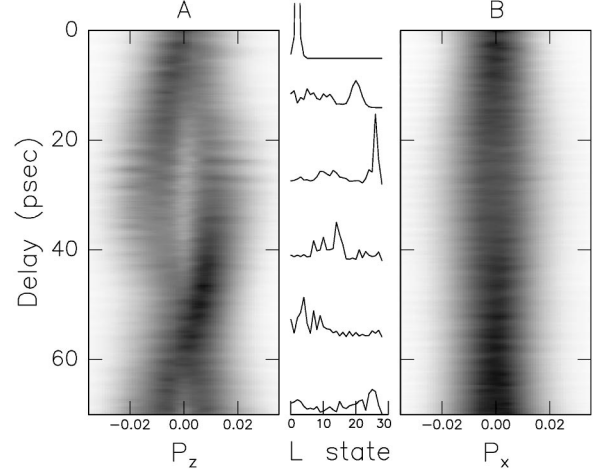


FIG. 1. Density plots of the measured time-dependent momentum distributions of the Stark wave packet in the (A)  $\hat{z}$  and (B)  $\hat{x}$  directions as described in the text. Dark indicates regions of high probability. The central inset shows the  $l$ -state composition of the wave packet at different times during its evolution.

ward. Ionization of electron probability that is moving in a direction opposite to the “kick” requires that the HCP field first reverse the electron’s motion, and then give it sufficient momentum to leave the atom. We bypass the need for high HCP fields by combining the ionization data obtained with positive and negative kicks along the same axis, e.g.,  $\hat{z}$  and  $-\hat{z}$ . Portions of the wave packet with positive momentum  $p_z > 0$  are easily ionized by a small impulse in the  $\hat{z}$  direction. Conversely, any part of the wave packet with  $p_z < 0$  is ionized with a weak kick in the  $-\hat{z}$  direction. Therefore, the positive and negative sides of the probability distribution are measured using oppositely polarized HCPs.

The measured projections of the wave packet’s momentum distribution parallel to the static field  $\hat{z}$  and perpendicular to the static field  $\hat{x}$  are shown in Figs. 1(A) and 1(B), respectively. The momentum axis is calibrated by scaling the bias voltage on the GaAs switch to the calculated impulse required to produce 50% ionization of the  $d$ -wave packet at  $t=0$  [3]. The temporal evolution of the two distributions is remarkably different. The distribution of momentum orthogonal to the field axis,  $D_x(t)$ , is nearly constant in time with only a few distinct time-dependent features, while  $D_z(t)$  shows an elaborate temporal progression. A symmetric breathing of  $D_x$  at the Kepler frequency appears as alternating light and dark patches near the center of the distribution, and is apparent just after the launch of the wave packet near  $t=0$  and at the first full return of the wave packet near  $t=\tau_S=54$  psec. These same oscillations appear with identical phase and frequency in  $D_z(t)$ , and are due to radial oscillations of the wave packet.  $D_x$  also exhibits a slight periodic breathing at the angular-momentum precession period  $\tau_S$ , so that  $D_x$  is 50% broader near  $t=\tau_S/2=27$  psec than at  $t=0$  or  $t=54$  psec.  $D_z$  shows a more dramatic long-term behavior. The single probability maximum that characterizes  $D_z$  at early times separates into two distinct peaks before collapsing back to a single feature at  $t=\tau_S$ . The maximum splitting in the probability doublet occurs near  $t=\tau_S/2$ .

The curves between Figs. 1(A) and 1(B) show the calcu-

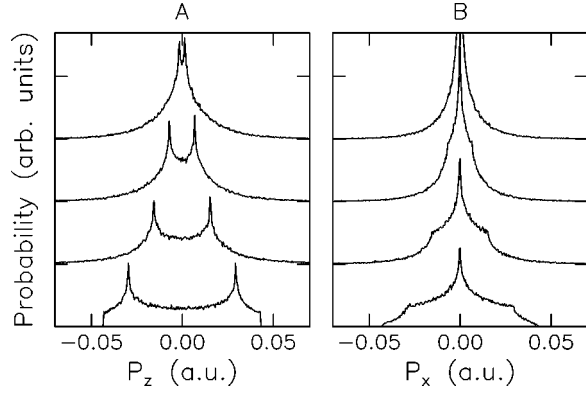


FIG. 2. Classical momentum distribution along (A)  $\hat{z}$  and (B)  $\hat{x}$  for hydrogenic  $n=28$ ,  $m_\ell=0$  states with (from top to bottom)  $\ell=2, 10, 20$ , and  $27$ .

lated distribution of probability among the orbital angular-momentum eigenstates at different times. Note that there is a clear progression of the angular momentum from  $\ell=2$  at  $t=0$  to  $\ell=n-1$  at  $t=\tau_S/2$  and back to low  $\ell$  at  $t=\tau_S$ . It is this angular-momentum progression that is the source of most of the structure in Figs. 1(A) and 1(B). For comparison, Figs. 2(A) and 2(B) show classical momentum distributions for the  $n=28$ ,  $m_\ell=0$ ,  $\ell=2, 10, 20$ , and  $27$  states in hydrogen. Note that the distribution along  $p_x$  is characterized by a single peak, centered about  $p_x=0$ , which broadens with increasing values of  $\ell$ . The Stark breathing of  $D_x$  in Fig. 1(B) is, therefore, a manifestation of the angular-momentum precession of the wave packet.

Figure 2(A) indicates that the splitting of  $D_z$  in Fig. 1(A) is also a direct reflection of the evolution of orbital angular momentum in the nonspherical potential. The bimodal,  $p_z$  component of the high- $\ell$  momentum distributions can be understood from classical physics as follows. For  $m_\ell=0$ , all classical trajectories lie in a plane that contains the  $z$  axis. Consequently,  $D_z$  gives an ‘‘end-on’’ view of an ensemble of planar orbits. For low-angular-momentum states, many orientations of the semimajor axis of the highly elliptical orbits relative to the  $z$  axis are possible, resulting in a broad momentum distribution that is peaked at zero. For circular orbits, however, there is only one orientation relative to the  $z$  axis. From an ‘‘end-on’’ view, there is a much larger probability of finding the electron moving along  $\hat{z}$  or  $-\hat{z}$  than in any other direction, and a double peaked distribution is produced. Conversely, most of the contribution to  $D_{x,y}$  comes from projecting the momentum of the electron out of its plane of motion. Therefore, there is always a maximum probability for having zero momentum along these axes, provided  $m_\ell=0$ . To our knowledge, the distributions in Fig. 1 represent the first observation of the angular-momentum dependence of bound electronic momentum distributions as well as the first direct measurement of the precession of angular momentum in Stark wave packets.

Closer inspection of Fig. 1(A) shows that the amplitudes of the positive and negative components of the bimodal  $D_z$  distribution are only equal at  $t=0$  and  $t=\tau_S$  when the wave packet has minimal angular momentum. For  $0 < t < \tau_S/2$ , the negative momentum component has the largest amplitude, while the positive peak is more prevalent for  $\tau_S/2 < t < \tau_S$ .

This asymmetry is related to the direction of travel of the electronic wave packet at its outer turning point and is easily described in terms of classical dynamics. At the time of its launch, the wave packet can be described as an ensemble of classical electrons traveling radially outward from the nucleus in a shell of probability. In addition to the central Coulomb restoring force, the electrons ‘‘feel’’ a noncentral ‘‘downhill’’ force,  $-F_S \hat{z}$  (a.u.), due to the static field. This force provides the torque responsible for angular-momentum precession in the field. The downhill force ensures that electrons that leave the nucleus with negligible angular momentum have a nonzero angular momentum and a velocity component in the  $-\hat{z}$  direction by the time they reach their mutual outer turning point  $R_0$ .

As shown in the center of Fig. 1 for  $0 < t < \tau_S/2$ , the angular impulse provided by the static field during each Kepler orbit tends to increase the angular momentum of each electron in the ensemble. Considering the discussion above, this implies that essentially all of the electrons in the ensemble have a common circulation, characterized by slow downhill motion near  $R_0$  and rapid uphill motion with great acceleration near the nucleus. Because the electron spends most of its orbit time near  $R_0$ , its momentum near  $R_0$  figures most prominently in the momentum distribution. Indeed, there is a pronounced negative momentum feature in Fig. 1(A) at  $0 < t < \tau_S/2$  due to the correlated circulation just described. For  $\tau_S/2 < t < \tau_S$ , the angular momentum of the wave packet is decreasing in time, indicating that the electron travels *uphill* ( $+\hat{z}$ ) near its outer turning point. Consequently, a positive peak in  $D_z$  is observed at these times.

At  $t=\tau_S/2$  the orbital angular momentum of the wave packet is maximal and the predominant electronic motion is nearly circular. As a result,  $D_z$  is perfectly symmetric with respect to the field direction when averaged over one Kepler period. However, Fig. 1(A) shows that the bimodal distribution near  $t=\tau_S/2$  is actually broken up by a strong antisymmetric momentum oscillation at the Kepler frequency. This rapid up and down shaking of the wave packet is a consequence of the same correlated motion that introduces the long-term up-down asymmetries in  $D_z$  at earlier and later times. Near  $t=\tau_S/2$ , the classical motion is that of an ensemble of electrons in nearly circular orbits that lie in a vertical plane. Each part of the packet moves uphill and then downhill in unison as it travels in its nearly circular trajectory. Cylindrical symmetry about the field axis ensures that equal amounts of electron probability move in the  $-\hat{x}$  and  $\hat{x}$  directions at all times. Consequently, no analogous ‘‘left-right’’ asymmetry or oscillation is expected or observed in  $D_x$ .

The rapid modulation in the probability distribution in Fig. 1(A) at  $t=\tau_S/2$  indicates a large-amplitude oscillation of the electric-dipole moment at the Kepler frequency, or 0.33 THz. This oscillating dipole emits THz radiation. The time-dependent radiated field is proportional to the measured electronic acceleration,  $d\langle p_z \rangle / dt$ , which is plotted in Fig. 3. The strong oscillations near  $t=27$  psec indicate that picosecond bursts of THz radiation are emitted by the atoms. Modification of this radiated field may be possible by changing the static field and/or the characteristics of the laser pulse that excites the wave packet [16].

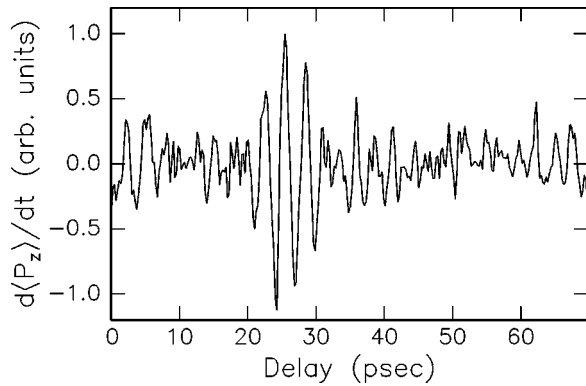


FIG. 3. Measured time dependence of the electron acceleration,  $d\langle P_z \rangle / dt$ , which is proportional to the field radiated by the wave packet during its evolution.

It should be noted that HCP ionization has been used to probe Stark wave packets previously [6,7]. In those experiments, oscillations in the ionization probability at both the Stark and Kepler periods were observed. Since no systematic measurement of ionization vs HCP field, delay, and orientation were made, the time-dependent momentum distribution could not be recovered. However, the observed modulations

were attributed to the time-dependent variations in the wave-packet momentum distribution. In one experiment [6], a clear “phase-shift” in the ionization feature associated with angular-momentum precession was seen for HCPs aligned with the static field, relative to antialigned fields, but no physical mechanism for the phase shift was proposed. Raman *et al.* [6] also observed that the Kepler oscillations in the ionization yield showed a relative  $\pi$  phase shift for aligned and antialigned HCPs. They attributed the fast antisymmetric modulation to polar angle oscillations of the wave packet at essentially constant radius. Those measurements and interpretation are consistent with our observations and the correlated circulation mechanism proposed here.

In summary, a complete measurement of the evolution of a Stark wave packet has been obtained. We have viewed the full precession of angular momentum of the electron, the effects of correlated circulation within the wave packet, and large THz oscillations of the electronic dipole moment along the applied static-field direction. Our measurement technique allows us to view the dynamics of complicated wave packets with high fidelity in real time.

We gratefully acknowledge the support of the AFOSR and the Packard Foundation.

- 
- [1] R. R. Jones and L. D. Noordam, *Adv. At., Mol., Opt. Phys.* **38**, 1 (1997), and references therein.
- [2] R. R. Jones, *Phys. Rev. Lett.* **76**, 3927 (1996); F. Robicheaux, *Phys. Rev. A* **56**, R3358 (1997).
- [3] M. B. Campbell, T. J. Bensity, and R. R. Jones, *Phys. Rev. A* **58**, 514 (1998).
- [4] T. C. Weinacht, J. Ahn, and P. H. Bucksbaum, *Phys. Rev. Lett.* **80**, 5508 (1998).
- [5] L. D. Noordam *et al.*, *Phys. Rev. A* **40**, 6999 (1989); B. Broers *et al.*, *Phys. Rev. Lett.* **71**, 344 (1993); G. M. Lankhuijzen and L. D. Noordam, *Phys. Rev. A* **52**, 2016 (1995); M. L. Naudéau, C. I. Sukenik, and P. H. Bucksbaum, *ibid.* **56**, 636 (1997).
- [6] C. Raman, T. C. Weinacht, and P. H. Bucksbaum, *Phys. Rev. A* **55**, R3995 (1997).
- [7] M. T. Frey *et al.*, *Phys. Rev. A* **55**, R865 (1997).
- [8] The quantum defect of the  $4snd \ ^1D_2$  levels is approximately  $\delta=1.1$  near  $n=28$ , so that the effective mean principal quantum number of the wave packet is  $N=26.9$ .
- [9] T. F. Gallagher, *Rydberg Atoms*, 1st ed. (Cambridge University Press, Cambridge, 1994).
- [10] D. You *et al.*, *Opt. Lett.* **18**, 290 (1993).
- [11] R. R. Jones, D. You, and P. H. Bucksbaum, *Phys. Rev. Lett.* **70**, 1236 (1993).
- [12] C. Raman *et al.*, *Phys. Rev. Lett.* **76**, 2436 (1996).
- [13] C. O. Reinhold *et al.*, *Phys. Rev. A* **54**, R33 (1996).
- [14] M. B. Campbell, T. J. Bensity, and R. R. Jones, *Opt. Express* **1**, 197 (1997).
- [15] N. E. Tielking, T. J. Bensity, and R. R. Jones, *Phys. Rev. A* **51**, 3370 (1995).
- [16] J. L. Krause and K. J. Schafer, *Opt. Express* **1**, 210 (1997).